ADVANCED FUNCTIONAL MATERIALS
www.afm-journal.de

Harnessing Multiple Folding Mechanisms in Soft Periodic Structures for Tunable Control of Elastic Waves

*Sicong Shan, Sung H. Kang, Pai Wang, Cangyu Qu, Samuel Shian, Elizabeth R. Chen, and Katia Bertoldi**

Mechanical instabilities in periodic porous elastic structures may lead to the formation of homogeneous patterns, opening avenues for a wide range of applications that are related to the geometry of the system. This study focuses on an elastomeric porous structure comprising a triangular array of circular holes, and shows that by controlling the loading direction, multiple pattern transformations can be induced by buckling. Interestingly, these different pattern transformations can be exploited to design materials with highly tunable properties. In particular, these results indicate that they can be effectively used to tune the propagation of elastic waves in phononic crystals, enhancing the tunability of the dynamic response of the system. Using a combination of finite element simulations and experiments, a proof-of-concept of the novel material is demonstrated. Since the proposed mechanism is induced by elastic instability, it is reversible, repeatable, and scale-independent, opening avenues for the design of highly tunable materials and devices over a wide range of length scales.

1. Introduction

Porous materials with well-defined periodicity are ubiquitous not only in nature, but also in synthetic structures and devices.[1] Periodic porous materials offer novel and unique properties, including light weight,[2] high energy absorption,[3] and the ability to control the propagation of both electromagnetic[4] and elastic waves[5,6] and heat flow.[7] The properties and functionality of such materials are generally determined by the deformation mechanisms of the ligaments, which buckle under compression at relatively low values of strain.

In elasto-plastic porous materials buckling of the beam-like ligaments results in collapse bands that progress at relatively constant stress, providing an efficient energy absorbing mechanism.[8–12] However, this deformation process cannot be exploited to dynamically tune the macroscopic response of the system, since it is irreversible. By contrast, in periodic porous elastic structures, buckling of the ligaments may trigger dramatic homogeneous and reversible pattern transformations.[13,14] Remarkably, it has been demonstrated that this parallel, cooperative buckling—a kind of "phase transition" from one to another microstructure—can be instrumental to design materials with tunable properties, including systems with tunable negative Poisson's ratio,[15] phononic[16–18] and photonic[19] switches and color displays.[20]

Most of the porous systems studied so far are dual-shaped, since mechanical instability is found to trigger only one distinct new buckled pattern. Although different buckling modes have been observed in hexagonal honeycombs under biaxial compression depending on the loading conditions,[1,9,10,21–23] the multiple pattern transformations induced by buckling have never been exploited to reversibly tune the properties of the system.

Here, we show that the ability to induce the formation of multiple ordered patterns in periodic porous elastic structures opens avenues for creating highly tunable systems. First, we develop a robust framework to identify periodic distributions of circular holes for which buckling and the direction of the applied loading can be exploited to form multiple folding patterns. Then, we confirm our findings through a combination of numerical simulations and experiments. Finally, we demonstrate numerically and experimentally that structures with multiple folding mechanisms open avenues for the design of highly tunable phononic crystals, whose response is effectively controlled by both the direction of loading and the magnitude of the applied deformation.

S. Shan, Dr. S. H. Kang, P. Wang, S. Shian, Dr. E. R. Chen, Prof. K. Bertoldi
School of Engineering and Applied Sciences
Harvard University
Cambridge, Massachusetts 02138, USA
E-mail: bertoldi@seas.harvard.edu
C. Qu
School of Aerospace
Tsinghua University
Beijing 100084, China
Prof. K. Bertoldi
Kavli Institute
Harvard University
Cambridge, Massachusetts 02138, USA

DOI: 10.1002/adfm.201400665

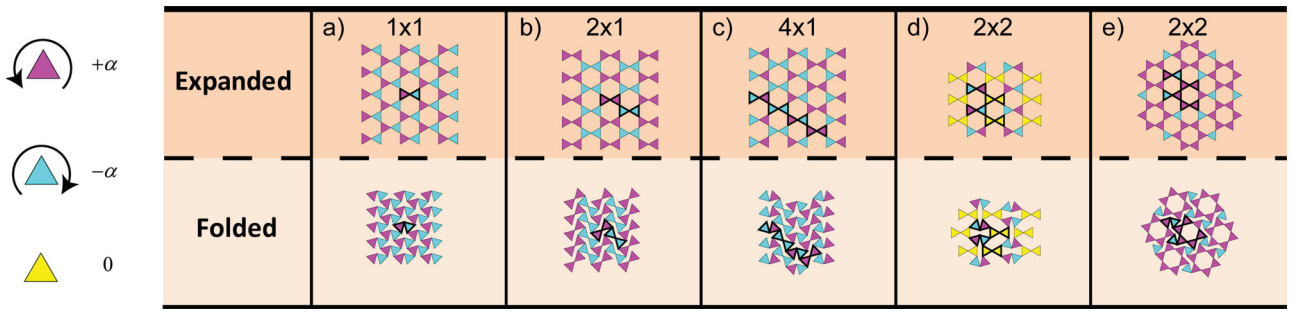

Figure 1. Schematic of the basic folding mechanisms in a rigid kagome network. The basic unit cell for each folding mechanism is outlined in black. The color of the triangles corresponds to their rotation. a) Mode with a basic cell of size 1 × 1; b) Mode with a basic cell of size 2 × 1; c) Mode with a basic cell of size 4 × 1; d) Mode with a basic cell of size 2 × 2; e) Mode with a basic cell of size 2 × 2.

2. Design of Soft Periodic Structures with Multiple Folding Mechanisms

2.1. Periodic Networks of Rigid Polygons

To identify periodic porous elastic structures with multiple folding mechanisms, we start by investigating the flexibility of periodic planar networks built from rigid corner-connected polygons, which can rotate freely. While a network of connected squares has a single folding mechanism (see Supporting Information), it has been recently shown that in planar networks built from equilateral triangles the number of folding mechanisms grows with the size of unit cell.[24] Here, we focus on the simplest of such tilings made of triangles – the kagome lattice. In this rigid network, the triangles are corner-connected to form hexagonal holes in the undeformed configuration and the smallest unit cell consists of only two triangles (see **Figure 1**-top).

If we consider a single unit cell (i.e. two corner-connected triangles) as a building block, it is easy to see that the periodic network has only one folding mechanism, in which all hexagonal holes progressively reduce to 3-point star-like shapes (see Figure 1a and Supporting Information). However, if we focus on a representative volume element (RVE) comprising an array of 1 × 2 unit cells (i.e. four corner-connected triangles) another folding mechanism emerges, resulting in a pattern of sheared voids where the shear direction alternates back and forth from row to row (see Figure 1b and Supporting Information). Finally, for a RVE consisting of 8 triangles, three other mechanisms are found: one consisting of alternating rows of sheared and 3-point star-like voids (see Figure 1c); another characterized by alternating rows of elongated holes oriented in horizontal and vertical direction and at ±30° with respect to the vertical direction (see Figure 1d); and a chiral pattern comprising six highly deformed voids surrounding an undeformed one (see Figure 1e).

Additional folding mechanisms can then be identified by considering larger RVEs (see Supporting Information). However, all these mechanisms share the same basic elements found in the patterns shown in Figure 1. We also note that in all the identified folding mechanisms the triangles are found either to rotate by $\pm\alpha$ (i.e. by the same amount either in clockwise or anti-clockwise direction, see magenta and cyan triangles in Figure 1) or not to rotate at all (i.e. $\alpha = 0$, see yellow triangles in Figure 1), facilitating the construction of folding mechanisms for large RVEs.

Finally, given the finite size of the elastomeric samples considered in this study, it is worth pointing out that we expect only the basic folding mechanisms shown in Figure 1 to be triggered during loading.

2.2. From Networks of Rigid Polygons to Continuum Porous Structures

Having found a planar network built from rigid corner connected triangles with multiple folding mechanisms, we then identify the corresponding porous structure. This can be easily done by replacing all the hexagonal voids with circular ones,[25] as shown in **Figure 2**. It is interesting to see that the outcome of this simple process is a porous structure comprising a periodic array of circular holes on a triangular lattice. In this continuum structure all the hinges of the original kagome network are replaced by thin ligaments and we expect these ligaments to buckle during loading.

Although the stability under biaxial compression of similar structures such as hexagonal honeycombs has been previously studied,[1,9,10,21–23] the ability to induce multiple pattern transformations has never been exploited to design materials and devices with enhanced tunability. In the next sections we investigate both numerically and experimentally how loading paths

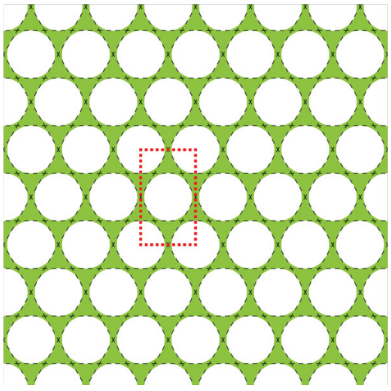

Figure 2. From a rigid networks of triangles to its corresponding continuum structure. All the hinges of the original kagome network (dashed black line) are replaced by thin ligaments in the continuum structure (shaded in green). The dotted red line indicates the unit cell of the structure.

with different angles can be exploited to trigger the different folding mechanisms shown in Figure 1, enabling the design of materials with highly tunable responses.

3. Mechanics of Soft Periodic Structures with Multiple Folding Mechanisms

3.1. Numerical Analysis

We continue by performing finite element (FE) simulations to investigate the patterns induced by buckling in a triangular array of circular holes in an elastomeric matrix. We focus on a structure characterized by an initial porosity $\Psi_0 = 70\%$ and assume plane strain conditions. The nonlinear finite-element code ABAQUS/STANDARD is used to deform the structures as well as to investigate its stability. For all the analyses, 2D finite element models are constructed using triangular quadratic elements (element type CPE6H in ABAQUS) and the accuracy of the mesh is ascertained through a mesh refinement study. Moreover, the response of the silicone rubber used in the experiments to cast the samples is captured using the incompressible Neo-Hookean hyperelastic model[26] with initial shear modulus μ_0.

Since the finite-sized specimens are necessarily influenced by boundary conditions at the edges, we focus on the response of the corresponding infinite periodic structure and study the response of rectangular RVEs by applying periodic boundary conditions.[27,28] We investigate the response of the porous structure under biaxial loading so that the macroscopic deformation gradient **F** is given by

$$\mathbf{F} = (1+\varepsilon_{xx})\mathbf{e}_x \otimes \mathbf{e}_x + (1+\varepsilon_{yy})\mathbf{e}_y \otimes \mathbf{e}_y + \mathbf{e}_z \otimes \mathbf{e}_z, \quad (1)$$

where ε_{xx} and ε_{yy} denote the macroscopically applied nominal strains and $\mathbf{e}_x$, $\mathbf{e}_y$ and $\mathbf{e}_z$ are the basis vectors of Cartesian coordinates.

Without loss of generality, we focus our attention to proportional straining paths in principal nominal strain space. More specifically, we assume that the ratio of the principal nominal strains is fixed, namely:

$$\varepsilon_{xx} = \lambda\cos(\theta), \varepsilon_{yy} = \lambda\sin(\theta) \quad (2)$$

where λ is the monotonically increasing load parameter and θ is the load path angle. In this study we consider $\pi \le \theta \le 3\pi/2$ to investigate various biaxial compression loading conditions. To facilitate the comparison between deformed configurations obtained for different values of θ, we also introduce the areal strain defined as[29]

$$\varepsilon_{Area} = \frac{A - A_0}{A_0} = (1+\varepsilon_{xx})(1+\varepsilon_{yy}) - 1 = \lambda(cos(\theta) + sin(\theta)) + \lambda^2 cos(\theta) sin(\theta) \quad (3)$$

A_0 and A denote the area of the RVE in the undeformed and deformed configuration, respectively.

To understand the patterns emerging as the result of buckling in the structure, we start by investigating the stability of the system. Taking the rectangular domain highlighted by red box in Figure 2 as unit cell, we consider RVEs consisting of $m \times n$ cells subjected to periodic boundary conditions. For a given value of θ we progressively load each RVE and calculate its natural frequency along the loading path, accounting for the effect of large deformation induced by loading. As an example, in **Figure 3**a we show the results of the stability analysis for an RVE comprising 2×2 unit cells and loading path angle $\theta = \pi$. In the undeformed configuration (i.e. $\lambda = 0$) all eigenvalues ω^2 are positive. However, as λ increases, the eigenvalues associated with each mode gradually decrease and eventually become negative. The critical loading parameter λ_{cr} associated with each mode can be easily extracted from the data, since it corresponds to the intersection point between each curve and the horizontal line $\omega^2 = 0$.

For this specific case, we find that the lowest critical loading parameter $\lambda_{cr,1} = 0.0331$ is associated with a mode that resembles the folding mechanism shown in Figure 1d for the kagome network. Here and in the following we refer to this mode as to the X-mode. The second mode is then triggered at $\lambda_{cr,2} = 0.0357$, resulting in a pattern similar to that reported in Figure 1b, which we denote as Z-mode. Subsequently, the third and fourth modes are found at $\lambda_{cr,3} = \lambda_{cr,4} = 0.0476$ consisting of alternating rows of sheared and 3-point star-like voids as that shown in Figure 1c. Finally the fifth mode is triggered at $\lambda_{cr,5} = 0.0665$, comprising an array of 3-point star-like voids as that reported in Figure 1a.

Identical calculations are then repeated for RVEs of different sizes and the critical strain of the infinite periodic structure for the given load path angle θ is then defined as the minimum of λ_{cr} on all possible periodic RVEs. In Figure 3b we report the critical strains for periodic RVEs with $m \times n$ cells for $\theta = \pi$. The results indicate that the critical loading parameter is the minimum for RVEs comprising an even number of unit cells in both directions and it is associated with the X-mode. Higher λ_{cr} is found for RVEs with an odd number of unit cells either in vertical or horizontal direction, for which the Z-mode is found to be critical. Therefore, when the structure is compressed with loading path angle $\theta = \pi$, we expect the X-mode to be triggered during loading.

Finally, to construct the instability surface we repeat the same calculations for different loading path angles θ. We first note that for all considered values of θ, the X- and Z-mode are always triggered either as first or second mode. In Figure 3c we then plot the critical load parameter associated with the X- and Z-mode as a function of θ. The critical load parameter λ_{cr} associated with the X-mode is found to decrease at first, to reach a minimum at $\theta = (5/4 - 1/36)\pi$ and then to progressively increase. Similar behavior is found for the critical loading parameter associated to the Z-mode, but in this case the minimum occurs at $\theta = (5/4 + 1/36)\pi$. Interestingly, for $\theta < 5\pi/4$ the critical loading parameter λ_{cr} associated to the X-mode is always lower than that corresponding to the Z-mode, so that the X-mode is expected to emerge during deformation for this range of loading path angles. By contrast, the Z-mode is expected to be triggered when $5\pi/4 < \theta < 3\pi/2$, since in this case the lowest critical loading parameter is that corresponding to the Z-mode. Finally, it is worth noting that both the X- and Z-mode are characterized by the same critical loading parameter for $\theta = 5\pi/4$, suggesting that for this specific loading

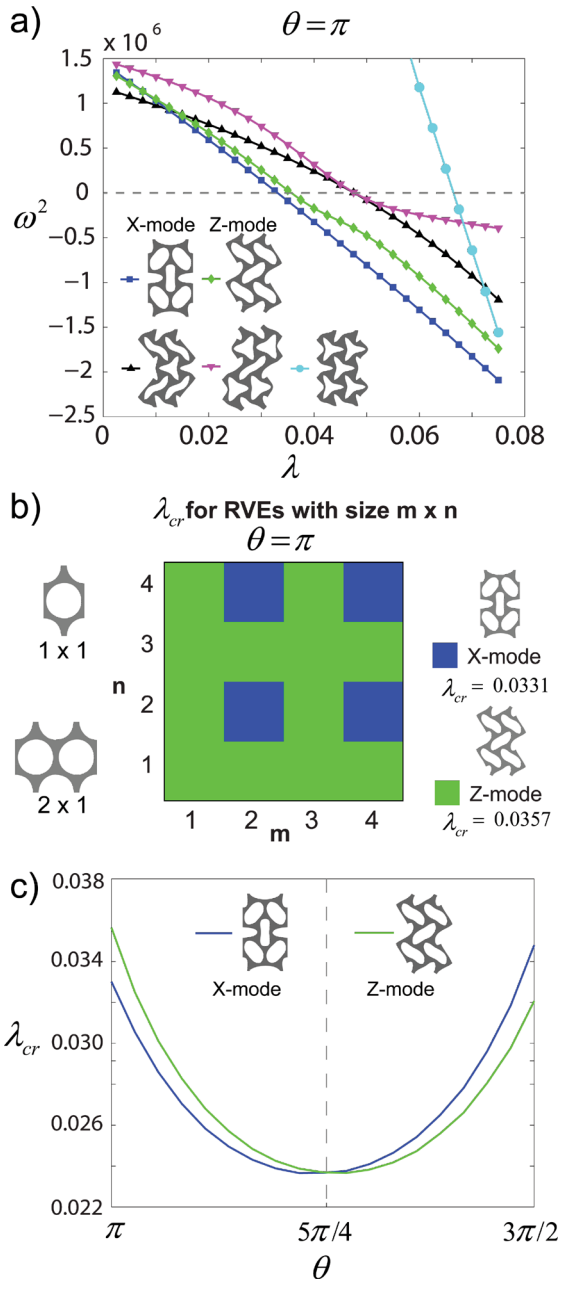

Figure 3. Numerical study of the instability of a periodic structure with multiple folding mechanisms. a) Evolution of eigenvalues at different levels of compression (loading along $\theta = \pi$ path) and corresponding deformation modes. The intersection points of each curve with the horizontal line $\omega^2 = 0$ corresponds to the critical loading parameter λ_{cr} for each mode. b) Critical loading parameter λ_{cr} for RVEs consisting of $m \times n$ unit cells (loading along $\theta = \pi$ path), where a unit cell consists of a rectangular domain with two voids. The results indicate that configurations with even number of unit cells along the two directions have the minimum critical strain. c) Critical loading parameter λ_{cr} associated to the X-mode (blue line) and Z-mode (green line) as a function of the loading path angle θ.

direction a pattern corresponding to a linear combination of both modes may be triggered.

Next, guided by the stability analysis we conduct a post buckling analysis on a RVE consisting of 2×2 unit cells by applying periodic boundary conditions and introducing a geometrical imperfection with the form of the first two eigenmodes. In **Figure 4**a, c and e we report numerical predictions of the pattern evolution for $\theta = \pi$, $5\pi/4$ and $3\pi/2$ at different values of areal strain ε_{Area}. Initially, the circular holes deform gradually and homogeneously. However, a transformation to a strikingly different pattern is triggered very early along the loading path (see images at $\varepsilon_{Area} = -0.05$) and the new patterns become further accentuated in shape with increasing strain as seen in the images at $\varepsilon_{Area} = -0.10$, -0.15, -0.20 and -0.25. As predicted by the stability analysis, the structure deforms into the X- and Z-mode when $\theta = \pi$ and $3\pi/2$, respectively.

However, a new chiral pattern resembling that reported in Figure 1e for the kagome network emerges when the structure is compressed equibiaxially (i.e. $\theta = 5\pi/4$). Interestingly, this chiral pattern does not correspond to one of the modes predicted by the stability analysis, but it can be obtained as a linear combination of the X- and Z-mode (see Supporting Information).

3.2. Experiments

To verify our numerical analysis, we fabricate centimeter scale elastomeric structures comprising 10×12 unit cells and characterized by initial porosity $\Psi_0 = 70\%$, hole diameter $D_0 = 8$ mm and out-of-plane thickness ~50 mm. The samples for the experiments are fabricated using silicone rubber (Mold Max 60 from Smooth-On Inc, Young's modulus $E = 2.16$ MPa) and a mold-casting process with molds prepared by 3D rapid prototyping. In-plane biaxial compression tests are performed using a custom-built testing set-up with four linear stages (see Supporting Information).

Representative pictures taken during the tests at different levels of ε_{Area} are presented in Figure 4b, d and f for $\theta = \pi$, $5\pi/4$ and $3\pi/2$, respectively. We start by noting that there is excellent agreement between numerical (Figure 4a, c and e) and experimental (Figure 4b, d and f) results. In particular, the effect of the boundary conditions is found to be negligible and the pattern transformations induced by instability are remarkably uniform across the samples, so that the behavior of the finite size sample does not deviate from that of the infinite periodic structure investigated numerically. Note that for the tests performed with $\theta = \pi$ and $\theta = 3\pi/2$, we do not constrain the deformation in lateral direction, since we find the lateral strain to be negligible (more specifically, we find the absolute value of lateral strain to be less than 0.05). Finally, since the specimens are made of an elastomeric material, the process is fully reversible and repeatable. Upon release of the applied loading condition, the deformed samples recover their original configurations, suggesting that this deformation mechanism can be exploited for the design of materials with tunable properties.

4. Harnessing Multiple Folding Mechanisms to Design Tunable Phononic Crystals

Having demonstrated that multiple folding mechanism can be easily triggered in a triangular array of circular voids by simply changing the loading path angle θ, in this section we show that the

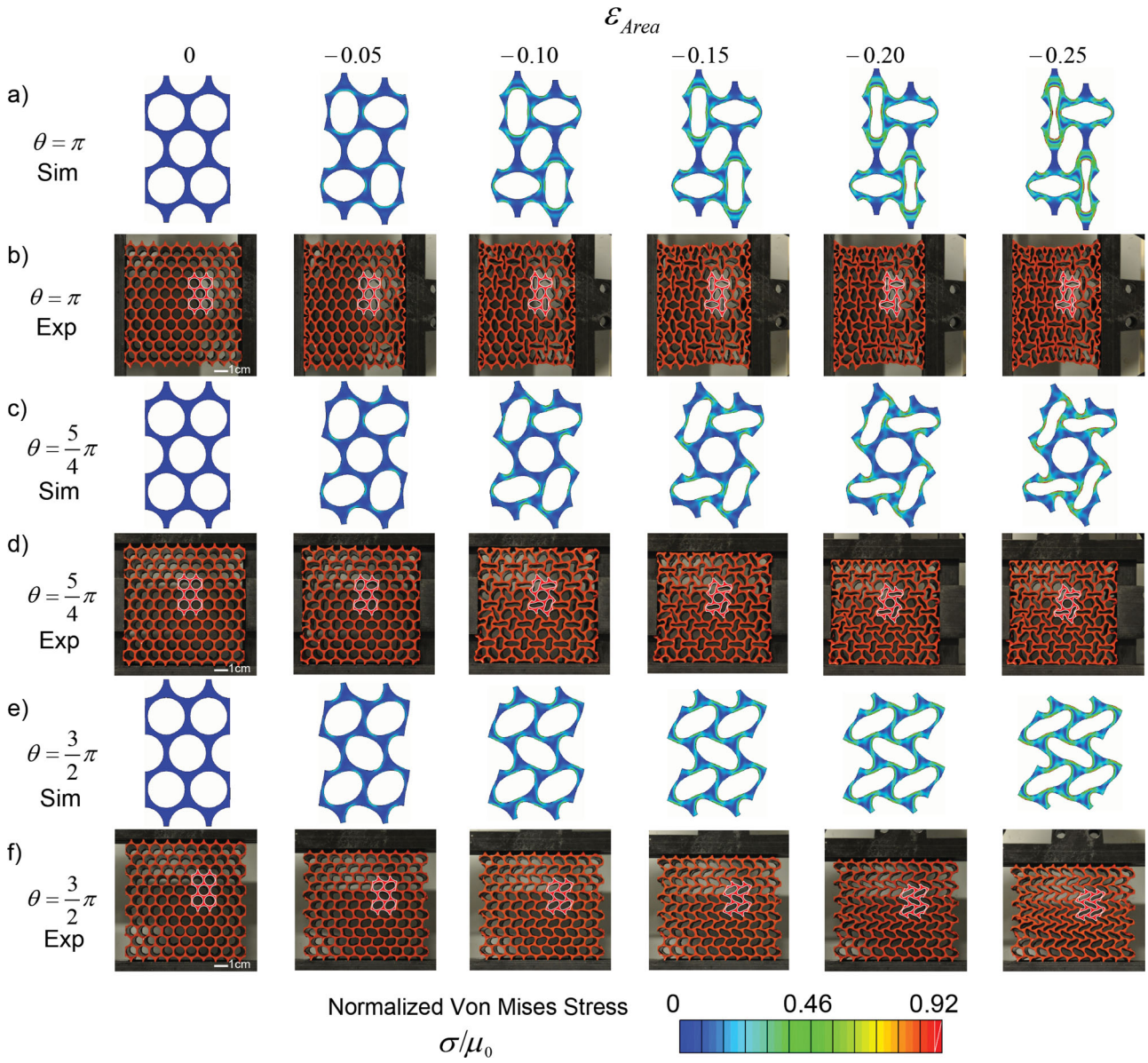

Figure 4. Numerical and experimental images of the triangular lattice loaded along $\theta = \pi$ (a and b), $\theta = 5\pi/4$ (c and d), $\theta = 3\pi/2$ (e and f) at different levels of deformation. The results show three distinct folding mechanisms: X-mode under horizontal compression (i.e. $\theta = \pi$), Z-mode under vertical compression (i.e. $\theta = 3\pi/2$) and a chiral mode under equibiaxial compression (i.e. $\theta = 5\pi/4$). The deformed shapes from simulation (colored in bright-red and outlined in white) are superimposed on the experimental pictures showing excellent agreement. For the numerical images, we also show the normalized Von Mises stress distributions in the deformed configurations.

system can be exploited to design highly tunable phononic crystals for the control and manipulation of elastic wave propagation.

Phononic crystals are periodic structures in which Bragg scattering is exploited to effectively filter elastic waves by the generation of bandgaps—frequency ranges of strong wave attenuation—at wavelengths comparable to the unit cell size.[5] Motivated by technological applications such as the design of waveguides,[30–36] frequency modulators,[31] noise reduction devices,[37–39] and vibration isolators,[40,41] the effects of both material properties,[42–44] and geometry (i.e., volume fraction and topology)[45,46] on the characteristics of phononic crystals have been investigated. Moreover, it has been recently recognized that large deformations induced by instabilities can be exploited to design phononic crystals whose bandgap position and width can be reversibly tuned.[16–18] Here, we show both numerically and experimentally that the tunability of the periodic system can be greatly enhanced in the presence of multiple folding mechanisms.

4.1. Numerical Analysis

To investigate the effect of different instability-induced patterns on the propagation of small amplitude elastic waves in

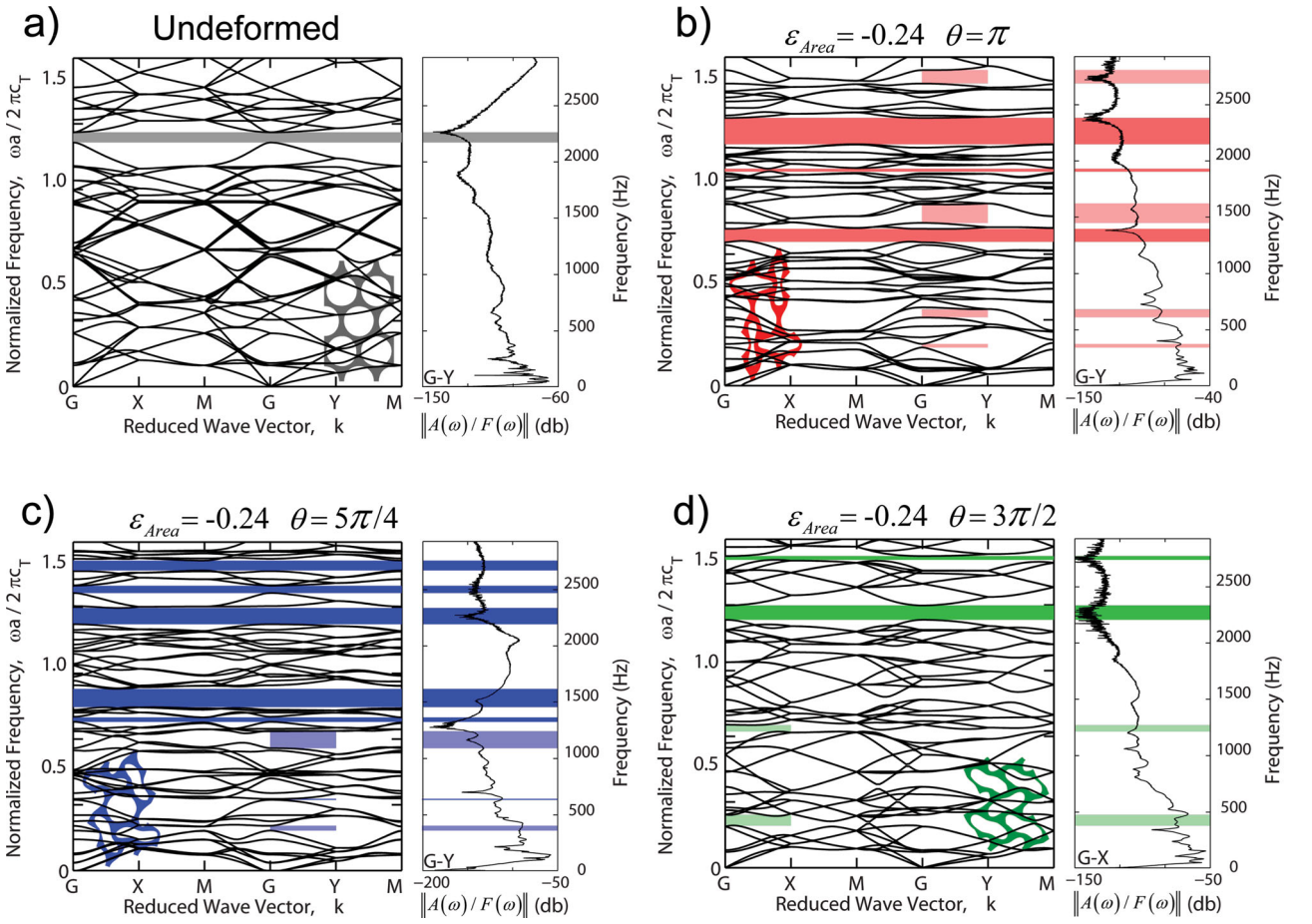

Figure 5. Comparison between the numerical dispersion relations (left) and the experimental frequency response functions (right) of the system obtained for different values of θ.

the periodic structure, we first conduct finite element analysis (see Supporting Information). We start by constructing the dispersion diagram for the undeformed configuration, as shown in **Figure 5**a. When undeformed, the periodic structure possesses a complete band gap (i.e. bandgap for all directions of wave propagation) for $\tilde{f} = \omega a/(2\pi c_T) = 1.189 - 1.238$, where ω is the angular frequency of the propagating wave, the lattice constant a = 10 mm is defined as the center-to-center distance between holes in the undeformed configuration and c_T = 18.3 m/s is the transverse speed of sound in the constituting homogeneous elastomeric material. Therefore, elastic waves with $f = \omega/(2\pi)$ in the range 2176–2266 Hz are not allowed to propagate within the undeformed structure due to the bandgap.

Next, we investigate the effect of the applied load on the propagation of elastic waves, by considering three deformed configurations obtained by different loading path angles $\theta = \pi$, $5\pi/4$ and $3\pi/2$, but under the same areal strain, ε_{Area} = –0.24. As shown in Figure 4, these three different values of q result in three distinct patterns. Interestingly, the dispersion diagrams shown in Figure 5-b, -c and -d indicate that the variation in patterns has a strong effect on the propagation of elastic waves, demonstrating that in periodic elastic structures with multiple folding mechanisms the band gaps can be dramatically altered not only by the extent of deformation but also by the choice of the loading path.

In fact, when the X-mode is triggered (i.e. $\theta = \pi$), the pre-existing complete band gap is shifted and widened to $\tilde{f} = 1.180 - 1.307$. In addition, two new complete band gaps that do not exist in the undeformed structure appear at $\tilde{f} = 0.699 - 0.765$ and $\tilde{f} = 1.045 - 1.070$. Differently, for $\theta = 5\pi/4$ the chiral folding mechanism is triggered and in this case the system is characterized by five complete band gaps for $\tilde{f} = 0.724 - 0.745$, $0.795 - 0.884$, $1.199 - 1.278$, $1.351 - 1.386$, and $1.461 - 1.509$. Finally, the Z-mode is triggered for $\theta = 3\pi/2$ and in this case the deformation is found to widen the pre-existing complete band gap and to open only one complete new band gap for $\tilde{f} = 1.207 - 1.277$.

4.2. Experiments

To validate the predictions of the numerical simulations, frequency response measurements of the elastomeric structure are made using an electro-dynamic shaker directly connected to one end of samples through a load cell to provide vibrations.

The dynamic response is recorded using a miniature accelerometer attached to the far end of the sample (see Supporting

Information). Measurements are conducted at different level of deformation and the transmittance is computed as the ratio between the output acceleration signal recorded at the far end of the sample and the input force signal from the load cell (i.e., $\left\|A(\omega)/F(\omega)\right\|$).

Figure 5 shows the comparison between numerical and experimental results. For each of the four panels in Figure 5, the dispersion plots on the left are calculated numerically and plots on the right show the transmittance curves from experiments. Here, the numerical calculations consider all propagation directions in an infinitely periodic structure, while the experimental results are shown for only one propagation direction (G-Y direction for Figure 5a, b and c; G-X direction for d). Nevertheless, we still observe a good match between these two sets of results. In the undeformed case, the experimental response indicates an apparent attenuation at the numerically calculated band gap frequency. After the structure is deformed into different patterns, the calculated complete band gaps can still find their signatures in the experimental results, with very few exceptions due to finite-size boundary effects that are not investigated in this study. Furthermore, the transmittance curves from experiments also exhibit some features of directional band gaps, indicated by the lighter color-shaded areas in Figure 5.

5. Conclusion

We demonstrated both numerically and experimentally the design of highly tunable phononic crystals by harnessing multiple folding mechanisms in periodic elastomeric structures comprising a triangular array of circular holes. We started with a geometrical analysis of 2D rigid periodic networks and found that a kagome lattice can have multiple folding mechanisms.

Guided by these results, we rationally designed the corresponding continuum soft periodic porous structure and showed that three different patterns induced by buckling can be triggered during compressive loading by changing the direction of loading. Remarkably, the dynamic response of the system was found to be highly affected by the pattern induced by buckling, demonstrating that the band gaps can be tuned both by deformation mode and the extent of deformation.

Our finding opens new opportunities to design multifunctional devices with enhanced tunability because (i) the mechanism can be applied to various length-scales; (ii) the various patterns can be triggered upon application of different stimuli and using different materials; (iii) the process is fully reversible and (iv) more importantly, the formation of different patterns can be easily controlled by changing the loading direction. By engineering geometry, length scales, and materials, we can envision smart systems that control the wave propagation autonomously depending on the loading conditions.

6. Experimental Section

Please see the Supporting Information for experimental details.

Supporting Information

Supporting Information is available from the Wiley Online Library or from the author.

Acknowledgements

This work has been supported by NSF through grant DMR-0820484 (Harvard MRSEC) and grant CMMI-1149456 (CAREER) and by the Wyss Institute through the Seed Grant Program. K.B. acknowledges start-up funds from the Harvard School of Engineering and Applied Sciences and the support of the Kavli Institute at Harvard University. E.R.C. acknowledges NSF MSPRF grant DMS-1204686. The authors wish to thanks Prof. David Clarke for the help with the experiments and Dr. Fillippo Casadei for useful discussions.

Received: February 26, 2014
Published online: May 19, 2014

[1] L. Gibson, M. Ashby, *Cellular Solids: Structure and Properties*, Cambridge University Press, Cambridge **1999**.
[2] T. Schaedler, A. Jacobsen, A. Torrents, A. Sorensen, J. Lian, J. Greer, L. Valdevit, W. Carter, *Science* **2011**, *334*, 962–965.
[3] J.-H. Lee, L. Wang, M. C. Boyce, E. L. Thomas, *Nano Lett.* **2012**, *12*, 4392–4396.
[4] D. Schurig, J. J. Mock, B. J. Justice, S. A. Cummer, J. B. Pendry, A. F. Starr, D. R. Smith, *Science* **2006**, *314*, 977–980.
[5] M. S. Kushwaha, P. Halevi, L. Dobrzynski, B. Djafari-Rouhani, *Phys. Rev. Lett.* **1993**, *71*, 2022–2025.
[6] M. Maldovan, E. L. Thomas, *Periodic Materials and Interference lithography for Photonics, Phononics and Mechanics*, Wiley-VCH, Weinheim **2009**.
[7] M. Maldovan, *Phys. Rev. Lett.* **2013**, *110*, 025902.
[8] T. Wierzbicki, W. Abramowicz, *J. Appl. Mech.* **1983**, *50*, 727–734.
[9] S. Papka, S. Kyriakides, *Int. J. Solids Struct.* **1999**, *36*, 4367–4396.
[10] S. Papka, S. Kyriakides, *Int. J. Solids Struct.* **1999**, *36*, 4397–4423.
[11] E. Wu, W. Jiang, *Int. J. Impact Eng.* **1997**, *19*, 439–456.
[12] A. M. Hayes, A. Wang, B. M. Dempsey, D. L. McDowell, *Mech. Mater.* **2004**, *36*, 691–713.
[13] T. Mullin, S. Deschanel, K. Bertoldi, M. C. Boyce, *Phys. Rev. Lett.* **2007**, *99*, 084301.
[14] Y. Zhang, E. A. Matsumoto, A. Peter, P. Lin, R. D. Kamien, S. Yang, *Nano Lett.* **2008**, *8*, 1192–1196.
[15] K. Bertoldi, P. Reis, S. Willshaw, T. Mullin, *Adv. Mater.* **2010**, *22*, 361–366.
[16] K. Bertoldi, M. C. Boyce, *Phys. Rev. B* **2008**, *77*, 052105.
[17] J. Jang, C. Y. Koh, K. Bertoldi, M. C. Boyce, E. L. Thomas, *Nano Lett.* **2009**, *9*, 2113–2119.
[18] P. Wang, J. Shim, K. Bertoldi, *Phys. Rev. B* **2013**, *88*, 014304.
[19] D. Krishnan, H. Johnson, *J. Mech. Phys. Solids* **2009**, *57*, 1500–1513.
[20] J. Li, J. Shim, J. Deng, J. T. B. Overvelde, X. Zhu, K. Bertoldi, S. Yang, *Soft Matter* **2012**, *8*, 10322–10328.
[21] L. Gibson, M. Ashby, J. Zhang, T. Triantafillou, *Int. J. Solids Struct.* **1989**, *31*, 635–663.
[22] J. Chung, A. Waas, *J. Eng. Mech.* **2001**, *127*, 180–193.
[23] N. Ohno, D. Okumura, H. Noguchi, *J. Mech. Phys. Solids* **2002**, *50*, 1125–1153.
[24] V. Kapko, M. Treacy, M. Thorpe, S. Guest, *Proc. R. Soc. A* **2009**, *465*, 3517–3530.
[25] J. Shim, S. Shan, A. Kosmrlj, S. H. Kang, E. R. Chen, J. C. Weaver, K. Bertoldi, *Soft Matter* **2013**, *9*, 8198–8202.
[26] R. W. Ogden, *Nonlinear Elastic Deformations*, Dover, New York **1998**.

[27] M. Danielsson, D. Parks, M. Boyce, *J. Mech. Phys. Solids* **2002**, *50*, 351–379.
[28] K. Bertoldi, M. C. Boyce, S. Deschanel, S. M. Prange, T. Mullin, *J. Mech. Phys. Solids* **2008**, *56*, 2642–2668.
[29] D. Needham, R. Nunn, *Biophys. J.* **1990**, *58*, 997–1009.
[30] A. Khelif, A. Choujaa, S. Benchabane, B. Djafari-Rouhani, V. Laude, *Appl. Phys. Lett.* **2004**, *84*, 4400–4402.
[31] M. Kafesaki, M. M. Sigalas, N. Garcia, *Phys. Rev. Lett.* **2000**, *85*, 4044–4047.
[32] A. Khelif, B. Djafari-Rouhani, J. O. Vasseur, P. A. Deymier, P. Lambin, L. Dobrzynski, *Phys. Rev. B* **2002**, *65*, 174308.
[33] J.-H. Sun, T.-T. Wu, *Phys. Rev. B* **2005**, *71*, 174303.
[34] J.-H. Sun, T.-T. Wu, *IEEE Ultrasonics Symposium* **2006**, *1*, 673.
[35] J.-H. Sun, T.-T. Wu, *Phys. Rev. B* **2007**, *76*, 104304.
[36] J. O. Vasseur, A. Hennion, B. Rouhani, F. Duval, B. Dubus, Y. Pennec, *J. App. Phys.* **2007**, *101*, 114904.
[37] D. Elser, U. L. Andersen, A. Korn, O. Glöckl, S. Lorenz, C. Marquardt, G. Leuchs, *Phys. Rev. Lett.* **2006**, *97*, 133901.
[38] T. Elnady, A. Elsabbagh, W. Akl, O. Mohamady, V. M. Garcia-Chocano, D. Torrent, F. Cervera, J. Snchez-Dehesa, *Appl. Phys. Lett.* **2009**, *94*, 134104.
[39] F. Casadei, L. Dozio, M. Ruzzene, K. Cunefare, *J. Sound. Vib.* **2010**, *329*, 3632.
[40] Y. Dian-Long, L. Yao-Zong, Q. Jing, Z. Hong-Gang, L. Zhi-Ming, *Chin. Phys. Lett.* **2005**, *22*, 1958.
[41] F. Casadei, B. Beck, K. A. Cunefare, M. Ruzzene, *Int. J. Solids Struct.* **2012**, *23*, 1169.
[42] D. Bria, B. Djafari-Rouhani, *Phys. Rev. E* **2002**, *66*, 056609.
[43] J. O. Vasseur, B. Djafari-Rouhani, L. Dobrzynski, M. S. Kushwaha, P. Halevi, *J. Phys. Condesed Mat.* **1994**, *6*, 8759.
[44] X.-Z. Zhou, Y.-S. Wang, C. Zhang, *J. App. Phys.* **2009**, *106*, 014903.
[45] J.-B. Li, Y.-S. Wang, C. Zhang, *J. Vib. Acoust.* **2013**, *135*, 031015.
[46] A. Movchan, N. Movchan, S. Haq, *Mat. Sci. Eng.* **2006**, *431*, 175183.